

## Electronic Supplementary Information

### Controlling Nucleation, Growth, and Orientation of Metal Halide Perovskite Thin Films with Rationally Selected Additives

Benjamin J. Foley,<sup>a</sup> Justin Girard,<sup>a</sup> Blaire A. Sorenson,<sup>b</sup> Alexander Z. Chen,<sup>a</sup> J. Scott Niezgoda,<sup>a</sup> Matthew R. Alpert,<sup>a</sup> Angela F. Harper,<sup>c</sup> Detlef-M. Smilgies,<sup>d</sup> Paulette Clancy,<sup>b</sup> Wissam A. Saidi,<sup>e</sup> and Joshua J. Choi<sup>a,\*</sup>

<sup>a</sup> Department of Chemical Engineering, University of Virginia, Charlottesville, Virginia 22904, USA.

<sup>b</sup> School of Chemical and Biomolecular Engineering, Cornell University, Ithaca, New York 14853, USA.

<sup>c</sup> Department of Physics, Wake Forest University, Winston-Salem, North Carolina 27109, USA.

<sup>d</sup> Cornell High Energy Synchrotron Source, Cornell University, Ithaca, New York 14853, USA.

<sup>e</sup> Department of Mechanical Engineering and Materials Science, University of Pittsburgh, Pittsburgh, Pennsylvania, 15261, USA.

\*Corresponding author. E-mail: [jjc6z@virginia.edu](mailto:jjc6z@virginia.edu)

### Computational Screening of Solvents and Additives

#### Mayer bond order

The MBO is computationally inexpensive to attain and is therefore well suited to high-throughput computational screening. Table S.1 shows the results of this survey of Mayer bond order and bond unsaturation values for THTO and eight other molecules that contain a sulfur-oxygen bond. Within the group of sulfoxide solvent molecules that we examined, tetrahydrothiophene 1-oxide, dimethyl sulfoxide, and methyl phenyl sulfoxide had the highest Mayer bond unsaturation values. Notably, these were the only solvents which contained a sulfur-oxygen double bond (S=O); each of the other molecules in the group either contained two S=O bonds, or a sulfur atom bonded to 4 oxygen molecules, as in the case of ethylene sulfite, diethyl sulfite, and dimethyl sulfate. Both ethylene sulfite and dimethyl sulfate had two of the highest MBO values (and hence lowest bond unsaturation values). Sulfur is hypervalent and can readily coordinate with lead to form a complex before being driven off during thermal annealing. One possible reason for diphenyl sulfoxide, which also contains a single S=O bond, to have a slightly higher MBO than THTO or DMSO is that the phenyl groups on this molecule are both electronegative, which reduces the strength of the S=O polarity in this molecule. This suggests that a major factor in the relative bond unsaturation of these atoms is the number of S=O bonds in the molecule.

**Table S.1.** Mayer Bond Order and the corresponding bond unsaturation values for nine solvents that contain a sulfur-oxygen bond. Results are provided for two levels of theory (B97-D3 and PWPB95). For this family of similar molecules, the lower the MBO, and the higher the bond unsaturation value, the better the efficacy of the solvent.

Solvent	MBO (Orca B97-D3 and PWPB95)		Bond Unsaturation (Orca B97-D3 and PWPB95)	
	B97-D3	PWPB95	B97-D3	PWPB95
Tetrahydrothiophene 1-oxide	1.61	1.48	0.39	0.52
Dimethyl sulfoxide	1.61	1.51	0.39	0.49
Methyl phenyl sulfoxide	1.63	1.52	0.37	0.48
Diphenyl sulfoxide	1.67	1.56	0.33	0.44
Dimethylsulfone	1.82	1.75	0.18	0.25
Diethyl sulfite	1.79	1.71	0.21	0.29
Tetramethylene sulfone	1.83	1.72	0.17	0.28
Ethylene sulfite	1.85	1.76	0.15	0.24
Dimethyl sulfate	1.93	1.83	0.07	0.17

Once the most accurate geometries were found for both the pure solvents and the  $\text{Pb}^{2+}$  solvent clusters, we calculated the enthalpy of solvation, as it is very closely related to the solubility of lead halides in polar solvents.  $\Delta H_{\text{solv}}$  is defined, thermodynamically, as the enthalpy released when a mole of the solute is moved from a vacuum to the solvent at infinite dilution. The enthalpy of solvation was calculated as follows, using the B97-D3 level of theory:

$$\Delta H_{\text{solv}} = E_{(\text{Pb} + \text{solvent})} - E_{\text{solvent}} - E_{\text{Pb}}$$

Where  $E_{(\text{Pb} + \text{solvent})}$  is the energy of the solvent and  $\text{Pb}^{2+}$  system,  $E_{\text{solvent}}$  the energy of the solvent cluster, and  $E_{\text{Pb}}$  the energy of the  $\text{Pb}^{2+}$  ion.

Table 1 in the main text shows the solvation enthalpy, as calculated for THTO and other commonly used solvents using the B97-D3 level of theory for comparison.

### MAPbI<sub>3</sub> thin film growth and morphology

Pictures were taken during the annealing process in a THTO saturated atmosphere to illustrate the extremely low nucleation density achieved by this method. (Figure S.1) The process shown below takes approximately 10 minutes from the time the film is placed on the hotplate to competition of crystallization. In this example, a petri dish was placed over the slide while the sample being annealed in order to slow the evaporation of THTO and further reduce the nucleation density. The SEM pictures of the microstructures as well as optical microscope pictures are shown in Figure S.2.

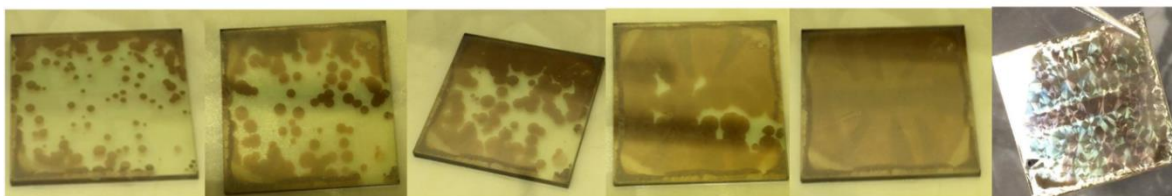


**Figure S.1.** MAPbI<sub>3</sub> forming from a MAPbI<sub>3</sub> precursor solution in a THTO saturated environment. The brown spots of MAPbI<sub>3</sub> grow together to form a film with full coverage. The substrate is 1 inch by 1 inch.

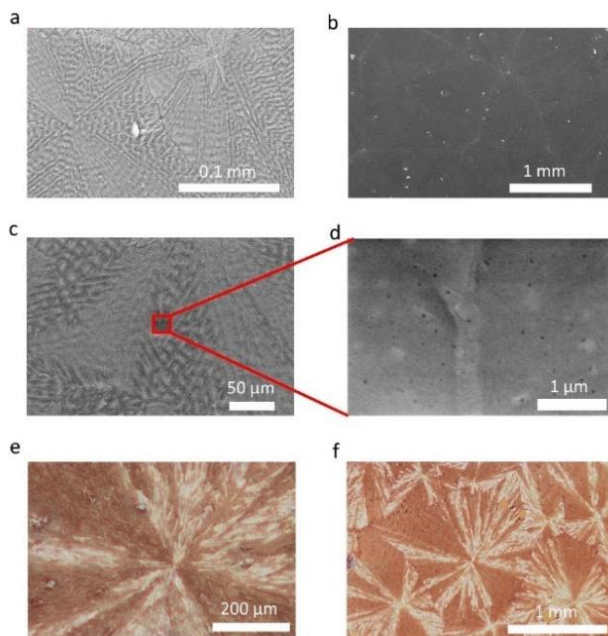


**Figure S.2.** (a), (b), (c) SEM images showing the macroscopic MAPbI<sub>3</sub> structures on PEDOT produced by the THTO additive method, as well as d) an image of the boundary between these structures taken at higher magnification. (e) and (f) optical images of the MAPbI<sub>3</sub> films.

### Temperature dependence of crystallographic orientation of thin films in the mixed halide method

MAPbI<sub>3</sub> film formation from the mixed halide precursor was studied *in-situ*, and it was found that the degree of preferential orientation gets reduced at lower temperatures, even though the precursor structure was the same. MAPbI<sub>3</sub> was deposited as described in the Experimental Details of the main text.

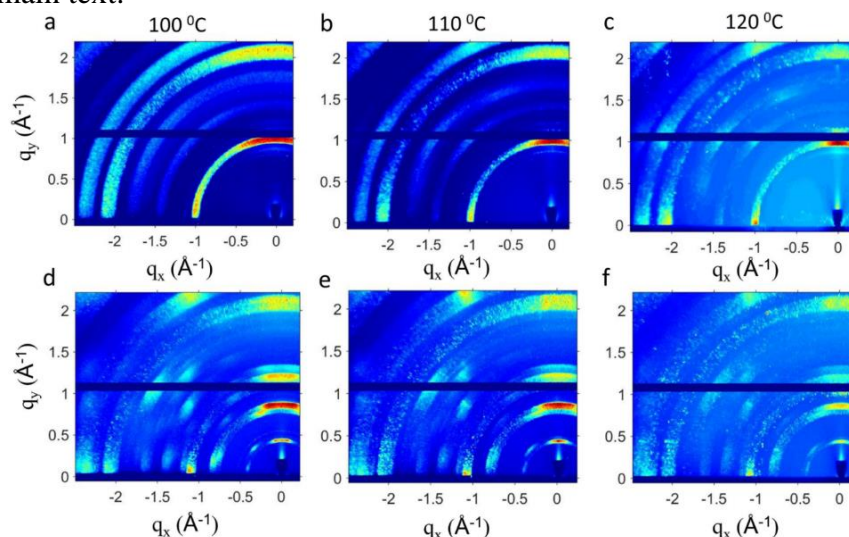


**Figure S.3.** (a), (b), (c) *In-situ* GIXD patterns for cubic MAPbI<sub>3</sub> films deposited using the mixed halide method<sup>1</sup> annealed at varying temperatures. (d) (e) (f) the precursor structures observed before MAPbI<sub>3</sub> formation for (a), (b), (c) respectively.

### Temperature dependence of crystallographic orientation of thin films in the THTO method:

MAPbI<sub>3</sub> formation from a THTO precursor solution was studied *in-situ*, and although the crystallization proceeds by the same mechanism, the degree of tetragonal (100) orientation is reduced as the temperature increases.

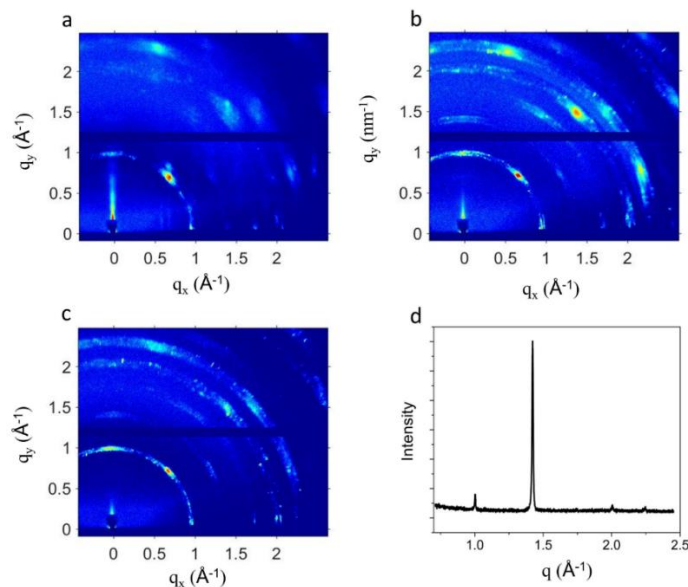


**Figure S.4.** GIXD patterns of MAPbI<sub>3</sub> deposited from THTO solution and annealed at (a) 70 °C, (b) 90 °C, (c) 110 °C, (d) 1D XRD pattern of MAPbI<sub>3</sub> deposited from THTO solution annealed at 140 °C.

### THTO concentration dependence of crystallographic orientation of thin films in the THTO method:

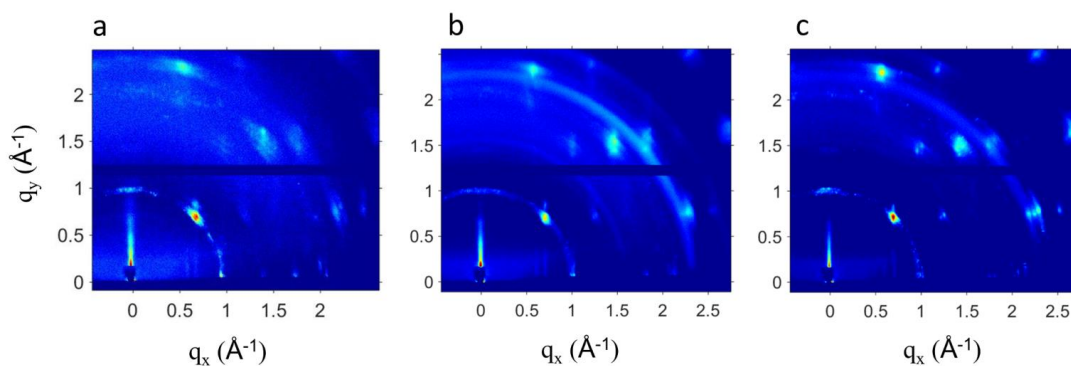


**Figure S.5.** GIXD patterns of MAPbI<sub>3</sub> thin film deposited from gBL solutions with (a) a 1:1 molar ratio of THTO:Pb, (b) a 3:1 molar ratio of THTO:Pb, and using pure THTO as the solvent. All films were fabricated on ITO/PEDOT and annealed at 70 °C. These results show that the degree of orientation is not sensitively dependent on THTO concentration.

### Reversible phase transitions

GIXD patterns of tetragonal (110) and (100) MAPbI<sub>3</sub> films on PEDOT:PSS were taken at 30 °C. The temperature was then ramped to 100 °C, held for 5 minutes, and another GIXD pattern was collected. The samples were then cooled back to 30 °C over approximately 30 minutes, and a final GIXD pattern was collected. These results show that the tetragonal-cubic phase transition is reversible in both orientations.

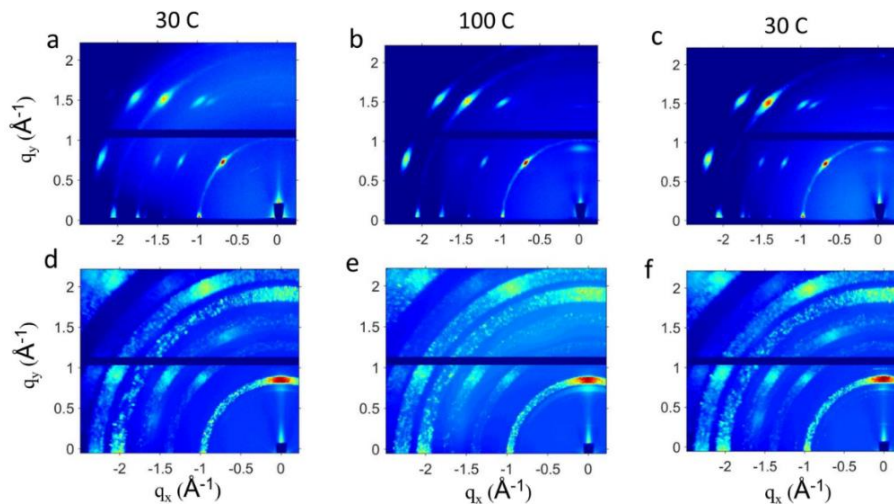


**Figure S.6.** GIXD patterns from tetragonal (100) film made using the THTO method when heated from (a) 30 °C to (b) 100 °C and cooled back to (c) 30 °C. The same procedure was carried out for tetragonal (110) films made using the mixed halide method<sup>1</sup>.

### Substrate dependence of morphology and orientation

MAPbI<sub>3</sub> was deposited as described in the Experimental Details on different substrates. There is a strong dependence of the morphology and surface coverage on the substrate type, and all substrates tested yield a much rougher morphologies than on the HTL formulation of PEDOT:PSS.

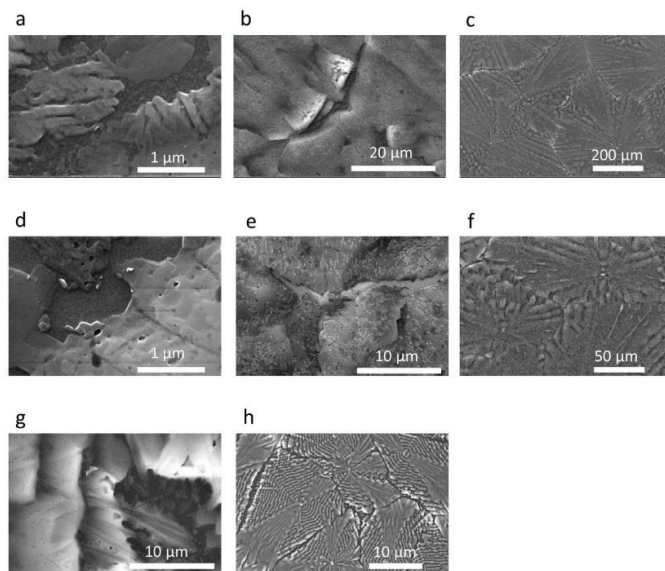


**Figure S.7.** MAPbI<sub>3</sub> films deposited using the THTO method on (a), (b), (c) TiO<sub>2</sub>, (d), (e), (f) NiO<sub>x</sub>, (g), (h) Al-4083 PEDOT:PSS. These films all appeared rough to the eye.

The substrate sensitivity is such that that even different formulations of PEDOT result in different thin film morphologies. The films imaged in Figure S.6 (g) and (h) were fabricated on the AI-4083 formulation and are much rougher than those fabricated on the HTL formulation (see Figure S.2)

To obtain smooth films, we found that the annealing MAPbI<sub>3</sub> layer deposited from THTO added precursor solution in a humid atmosphere (40-70 % relative humidity) is helpful. Alternatively, adding 100 uL/mL of deionized water to the precursor solution was also helpful. Even though the overall morphology and roughness of the film is affected by the presence of water, the tetragonal (100) orientation is robustly obtained with or without any water whenever THTO is added to the precursor solution on all substrates shown above.

### **Analysis of X-ray Incidence Angle Dependence**

The stability of the THTO-added MAPbI<sub>3</sub> precursor solution at room temperature and slow crystallization allow multiple XRD patterns to be taken at different angles during the crystallization process. In order to determine if crystal growth starts at the air/solution interface or the substrate/solution interface, the intensities of the Bragg peaks at different X-ray incident angles while the crystal was growing were compared to the intensity after growth was complete.

The precursor solution was spin-coated onto an ITO/PEDOT:PSS substrate at 2500 rpm for 30 seconds. The sample was then placed on the sample stage at room temperature and aligned to the X-ray beam. The temperature of the sample was then ramped to 70 °C over 30 seconds, and data collection was started when the sample temperature reached 70 °C. Diffraction patterns were taken at sample to beam incident angles of 0.1, 0.25, and 0.5 degrees. At 0.1 degree, no ITO peaks (a ring at  $q = 2.3 \text{ \AA}^{-1}$ ) were visible, verifying that the substrate/perovskite interface was sampled weakly. At 0.25 degrees, the ITO peaks were faintly visible, and at 0.5 degrees a strong ITO peak was present, verifying the substrate/perovskite interface is being sampled strongly. The ITO peak, present in the GIXD patterns as a ring at  $q = 2.3 \text{ \AA}^{-1}$ , can be seen in Figure S.7 (c) and (f). As the intensity of Bragg peaks from MAPbI<sub>3</sub> increases as the crystal forms, the relative intensity of the MAPbI<sub>3</sub> peaks at the different X-ray incidence angles is of interest.

The angle-dependence of the intensity was collected while the crystals were nucleating and growing, as determined by the first appearance of MAPbI<sub>3</sub> peaks, and it was observed that the MAPbI<sub>3</sub> peaks appeared at the deeper angles before they appear in shallower angles. (Figure S.6 (a), (b), (c)) The same trend at a later time during the initial MAPbI<sub>3</sub> nucleation (Figure S.7 (d), (e), (f)) indicates that the intensity variation is due to the angle and not the lag time between measurements at each of these different angles.

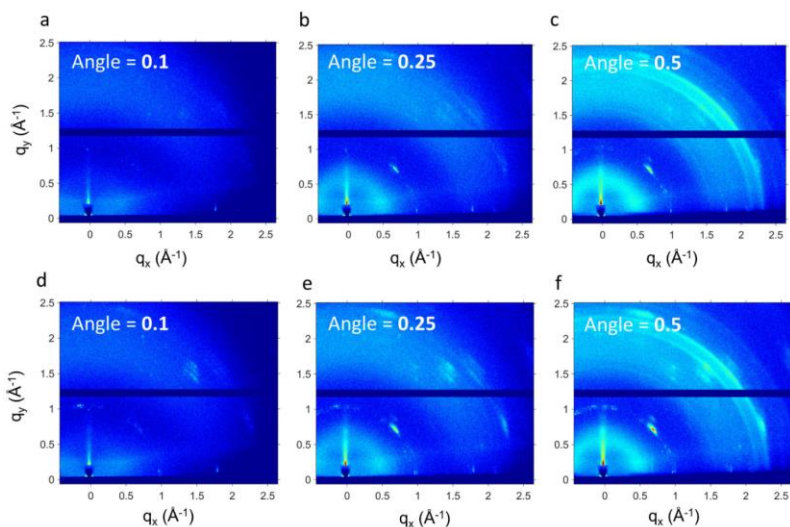


**Figure S.8.** (a), (b), (c) angular dependence of the X-ray diffraction pattern when the MAPbI<sub>3</sub> peak was first observed, (d), (e), (f) the angular dependence 12 seconds after (a), (b), (c) were taken. It can be seen that the MAPbI<sub>3</sub> peak is only visible at the steeper angles, where the ITO peak, which appears as a ring at  $q = 2.3 \text{ \AA}^{-1}$ , is also visible.

The peak intensities were also compared quantitatively, which confirm the trend. The ratio of the intensity at steeper angles to that of shallower angles (intensity at 0.25° or 0.5° divided by intensity at 0.1°) is very high initially, and then decreases as crystallization proceeds. Figure S.8 shows the ratios of intensities (with the background subtracted) at incident angles of 0.1° to angles of 0.25° or 0.5° for 8 sequences during crystallization.

If nucleation occurs at the substrate/precursor solution interface, then the peak intensity will be higher at steeper angles. The variability with respect to angle should decrease as crystallization is completed, as the beam will encounter MAPbI<sub>3</sub> crystals instead of precursors in the solution. Our results show this trend and, together with the substrate dependence of the process, they indicate that the MAPbI<sub>3</sub> crystal nucleates at the substrate/solution interface.

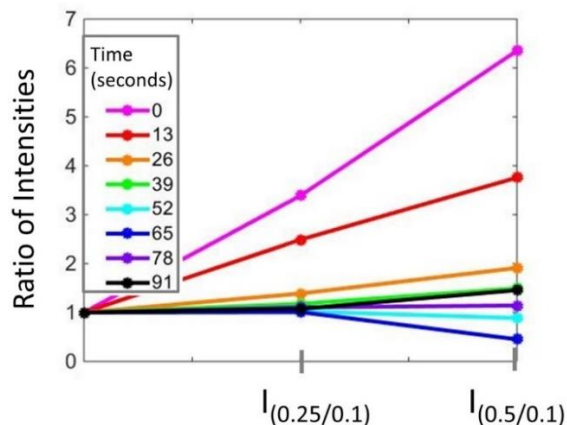


**Figure S.9.** Cubic (110) peak intensity at incident angles of 0.25 and 0.5 degrees normalized to the intensity at an incident angle of 0.1 degree during the nucleation of MAPbI<sub>3</sub> from THTO added precursor solution. The background was subtracted before normalizing. Each series of three angles was collected at a different time, as denoted by the legend, with zero being the time the first peak was observed, not the start of annealing.

### Robustness of tetragonal (100) orientation against changing the substrate

As mentioned in the main text, the tetragonal (100) or cubic (110) orientation is robust across all substrates tested. The XRD patterns from MAPbI<sub>3</sub> thin film deposited from THTO added precursor solution on SiO<sub>2</sub>, TiO<sub>2</sub>, Si and NiO<sub>x</sub> are shown in Figure S.9.

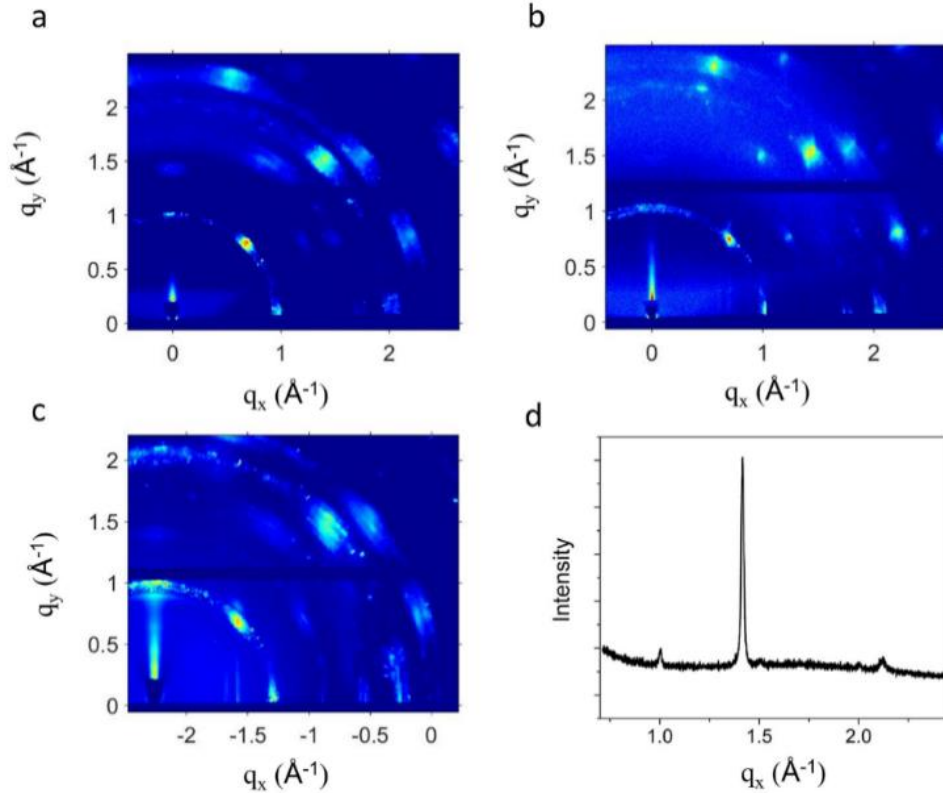


**Figure S.10.** Tetragonal (100) oriented films deposited using the THTO method on a) SiO<sub>2</sub> b) TiO<sub>2</sub> c) Si d) NiO<sub>x</sub>

### Details and additional results from DFT calculations of surface energies

#### Calculation of surface energies:

The surface energies were calculated using a grand canonical approach<sup>2</sup>, which has terms allowing the calculation of non-stoichiometric surfaces. Entropic effects are neglected, and as the surfaces are quite similar, are unlikely to influence the conclusions drawn from these calculations.

$$\Omega(\Delta\mu_{\text{Pb}}, \Delta\mu_{\text{I}}, \Delta\mu_{\text{MAPbI}_3}) \approx E_{\text{tot}}[\text{Pb}_\alpha\text{I}_\beta(\text{MAPbI}_3)_\gamma] - \alpha\mu_{\text{Pb}}^{\text{bulk}} - \frac{\beta}{2}\mu_{\text{I}_2}^{\text{gas}} - \gamma\mu_{\text{MAPbI}_3}^{\text{bulk}} - \alpha\Delta\mu_{\text{Pb}} - \beta\Delta\mu_{\text{I}}$$

where  $\mu$  is the chemical potential, approximated as the DFT energy,  $\gamma$  is the number MAPbI<sub>3</sub> units,  $\alpha$  is the total Pb atoms minus  $\gamma$ , and  $\beta$  is the total number of iodine atoms minus  $3*\gamma$ .  $\Omega$  is the grand potential.

**Table S.2. Comparison of surface energies calculated in this work and by Haruyama *et al.*<sup>2</sup>**<sup>a</sup>

Termination	$\Omega/s$ (eV/nm <sup>2</sup> ), This work	$\Omega/s$ (eV/nm <sup>2</sup> ), Haramunya <i>et al.</i>
100 (PbI <sub>2</sub> ) <sub>2</sub>	3.57	3.31
100 (PbI <sub>4</sub> ) <sub>2</sub>	2.03	1.73
100 (PbI <sub>5</sub> ) <sub>2</sub>	0.89	0.74
100 (PbI <sub>6</sub> ) <sub>2</sub>	5.24	4.91
110 (PbI <sub>5</sub> ) <sub>2</sub>	3.68	3.4
110 (PbI <sub>5</sub> ) <sub>2</sub> PbI <sub>3</sub>	2.25	1.61
110 (PbI <sub>5</sub> ) <sub>4</sub>	1.38	1.25
100 PbI <sub>5</sub> PbI <sub>3</sub>	1.09	0.92

<sup>a</sup> Surface energies were calculated at  $\Delta\mu_{\text{Pb}} = -1.19$  and  $\Delta\mu_{\text{I}} = -0$ .

The Van der Waals correction was not included, following Haruyama *et al.*<sup>2</sup> who found it not to significantly affect the surface energies. The surface energies listed from Haruyama *et al.*,<sup>2</sup> used the rev-vdW-DF functional, and so are only roughly comparable to ours. Our results are consistently higher by 0.1-0.2 eV, but the energies of the terminations relative to one another are consistent (our most stable surface is the most stable surface found by Haruyama *et al.*, etc). Four tetragonal (110) surfaces, four tetragonal (100) surface, four cubic (100) surfaces and five cubic (110) surfaces were examined. The supercell sizes are indicated in Tables S.3 and S.4.

We note that, when comparing computational DFT results to experiments, the trend in calculated values is more reliable than the absolute values. For both the bare surfaces and THTO bound surfaces, a stoichiometric cubic (110) surface was calculated to be more stable, followed by a stoichiometric cubic (100) surface., and we do not make any conclusions based on comparing the absolute values calculated from different structural configurations. Instead, given the same supercell configuration, we focus on how much the surface energies change with THTO binding. Our DFT results show that THTO stabilizes the cubic (110) surface significantly more than the cubic (100) surface.

### Surface energy diagrams for cubic and tetragonal structures with or without THTO:

The phase diagrams below show the most stable (lowest energy) and second most stable tetragonal surfaces with and without THTO. The difference between those surfaces is listed on the figure. The chemical potential of Pb and I is not known under experimental conditions, therefore it is a common practice to examine the stabilities in the entire region where formation of the

$$\Delta H_{\text{form}}[\text{MAPbI}_3] - \Delta H_{\text{form}}[\text{MAI}] \leq \Delta\mu_{\text{Pb}} + 2\Delta\mu_{\text{I}} \leq \Delta H_{\text{form}}[\text{PbI}_2]$$

compound is thermodynamically favorable. As such, the most stable termination varied  $\Delta\mu_I$  and  $\Delta\mu_{Pb}$ . The criteria for stability are listed below<sup>2</sup>:

$$\Delta H_{\text{form}}[\text{MAPbI}_3] \leq \Delta\mu_{Pb} \leq 0 \quad \Delta H_{\text{form}}[\text{MAPbI}_3] \leq \Delta\mu_I \leq 0$$

The boundaries between different surfaces are denoted by the dashed lines, and the region of stability by solid lines.

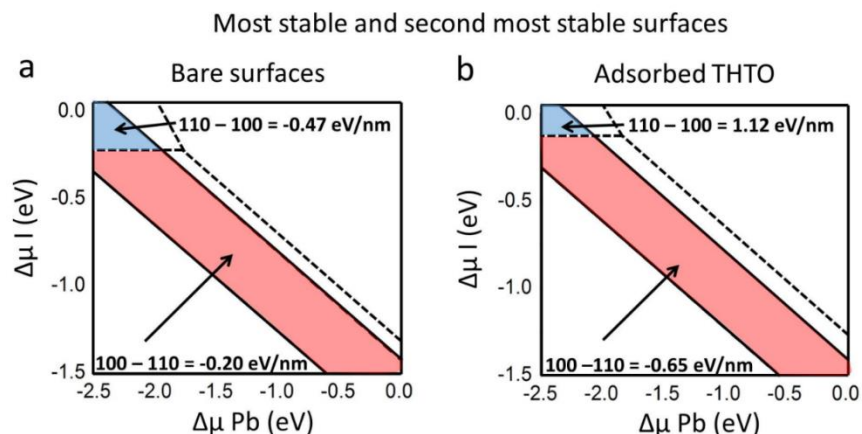


**Figure S.11.** The first and second most stable surfaces, and the difference between them (the most stable is listed first). Of the three regions shown on the phase diagram, only the two which fall within the region of stability are labeled. Note that in the small blue region in the adsorbed THTO phase diagram, the difference between the surfaces is negative, indicating that the tetragonal (100) orientation is the more stable.

As can be seen from Figure S.10 (a) and (b), adsorption of THTO changes the lowest energy surface from tetragonal (110) to tetragonal (100) in the iodide rich (upper left) portion of the phase diagram. For the rest of the region of stability, the tetragonal (100) surface is only 0.2 eV more stable than the competing tetragonal (110); this difference increases to 0.4 eV upon adsorption of THTO. While it is not known why the tetragonal (100) is predicted to be more stable, as also calculated by Haruyama *et al.*<sup>2</sup>, when the tetragonal (110) is more commonly observed experimentally. This does not discredit that the trend clearly shows binding of THTO stabilizes the tetragonal (100) more than the tetragonal (110). We note that, when comparing computational DFT results to experiments, the trend in calculated values is more reliable than the absolute values and we do not make any conclusions based on comparing the absolute values calculated from different structural configurations. Instead, we focus on, given the same supercell configuration, how much the surface energies change with THTO binding. Our calculations support the conclusion that the binding of THTO alters the surface energies such that the tetragonal (100) (cubic 110) is more stabilized under the experimental conditions yielding the tetragonal (100) orientation.

The impact of THTO on surface stability for the tetragonal phase is shown below using the same presentation as the reconstructed cubic phase was given in the main text in Figure 4. Figure S.11 is a comparison of the most stable tetragonal phases for the red region of the phases diagram shown in Figure S.10.

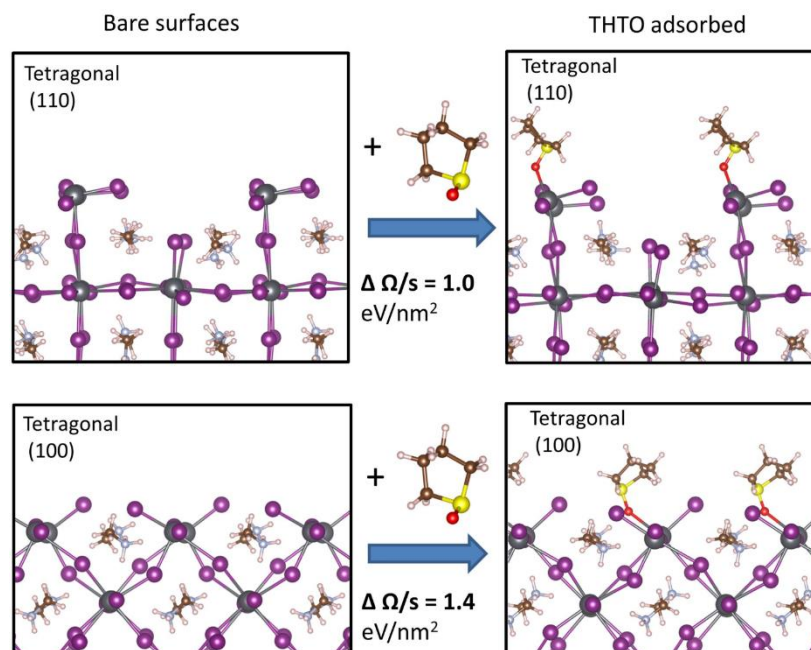


**Figure S.12.** The two most stable tetragonal surfaces of MAPbI<sub>3</sub> with and without THTO calculated with density functional theory. The surface energy is denoted by  $\Omega/s$ . The calculations show that adsorbing THTO stabilizes the tetragonal (110) surface by 1.0 eV/nm<sup>2</sup>, while the tetragonal (100) is only stabilized by 1.4 eV/nm<sup>2</sup>.

The phase diagrams for the cubic system are shown below. A stoichiometric cubic (110) surface is the lowest energy surface in the entire region of stability. It can be seen that the difference in energy increases by 0.3 eV when THTO adsorbs and the cubic (110) is stabilized more than the cubic (100).

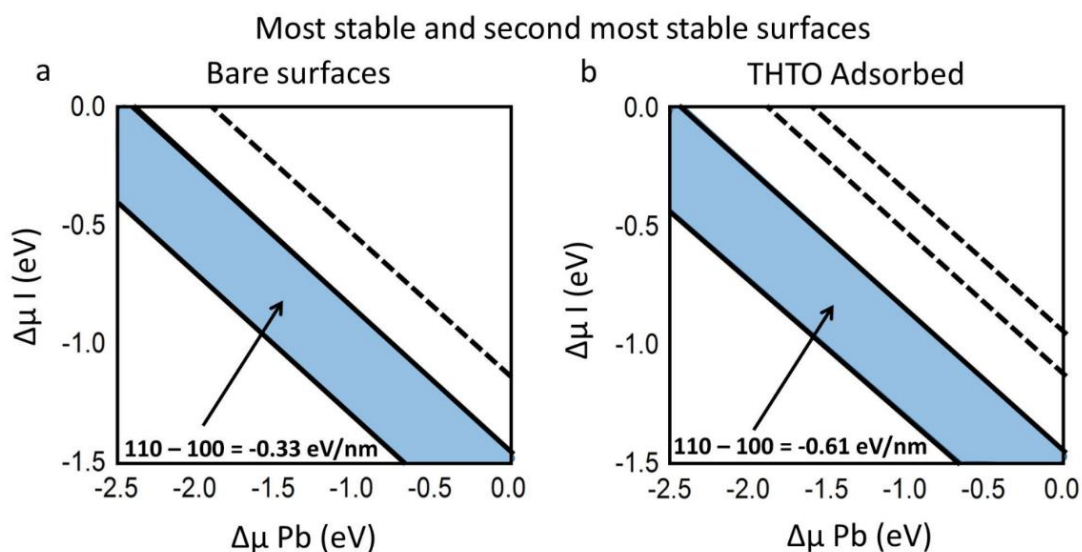


**Figure S.13:** phase diagrams for the cubic system with and without THTO.

**Lattice constants and calculated surface energies:**

Optimized bulk cubic structure:  $a = 6.360 \text{ \AA}$ , all cubic surfaces were constructed from this unit cell. For the tetragonal phase, the same lattice constants as reported by Haruyama *et al.*<sup>2</sup> for the optimization performed using the PBE functional.

**Table S.3 Lattice constants, stoichiometry, surface energies, and THTO binding energies for the cubic surfaces.**

	Cubic Surfaces	Stoichiometry	$\Omega/S$ THTO (eV/nm <sup>2</sup> )	$\Omega/S$ Bare surface (eV/nm <sup>2</sup> )	THTO Binding Energy (eV)
a = 1.272 nm <sup>2</sup> b = 0.636 nm <sup>2</sup>	100	I <sub>2</sub> (MAPbI <sub>3</sub> ) <sub>12</sub>	2.57	4.04	-1.19
	100	Pb <sub>2</sub> I <sub>2</sub> (MAPbI <sub>3</sub> ) <sub>12</sub>	5.84	6.81	-0.78
	100	Pb <sub>2</sub> I <sub>4</sub> (MAPbI <sub>3</sub> ) <sub>12</sub>	1.94	3.73	-1.45
	100	(MAPbI <sub>3</sub> ) <sub>12</sub>	0.61	1.95	-1.09
a = 1.272 nm <sup>2</sup> b = 0.899 nm <sup>2</sup>	110	Pb <sub>4</sub> I <sub>8</sub> (MAPbI <sub>3</sub> ) <sub>14</sub>	3.26	4.40	-0.97
	110	Pb <sub>4</sub> I <sub>4</sub> (MAPbI <sub>3</sub> ) <sub>14</sub>	6.74	9.73	-1.30
	110	(MAPbI <sub>3</sub> ) <sub>14</sub>	0.00	1.62	-1.76
	110	I <sub>4</sub> (MAPbI <sub>3</sub> ) <sub>14</sub>	2.64	4.71	-1.16

**Table S.4 Lattice constants, stoichiometry, surface energies, and THTO binding energies for the tetragonal surfaces**

	Tetragonal Surfaces	Stoichiometry	$\Omega/S$ THTO (eV/nm <sup>2</sup> )	$\Omega/S$ Bare surface (eV/nm <sup>2</sup> )	THTO Binding Energy (eV)
a = 1.299 nm <sup>2</sup> b = 0.900 nm <sup>2</sup>	100	Pb <sub>4</sub> I <sub>4</sub> (MaPbI <sub>3</sub> ) <sub>14</sub>	5.39	3.57	-1.51
	100	Pb <sub>4</sub> I <sub>8</sub> (MaPbI <sub>3</sub> ) <sub>14</sub>	1.93	2.03	-1.38
	100	(MaPbI <sub>3</sub> ) <sub>14</sub>	-0.53	0.89	-1.66
	100	I <sub>4</sub> (MaPbI <sub>3</sub> ) <sub>14</sub>	1.08	5.24	-2.49
a = 1.299 nm <sup>2</sup> b = 1.263 nm <sup>2</sup>	110	I <sub>4</sub> (MAPbI <sub>3</sub> ) <sub>24</sub>	1.44	3.68	-1.30
	110	Pb <sub>2</sub> I <sub>4</sub> (MAPbI <sub>3</sub> ) <sub>24</sub>	1.52	2.25	-1.83
	110	Pb <sub>4</sub> I <sub>8</sub> (MAPbI <sub>3</sub> ) <sub>24</sub>	1.93	1.38	-1.61
	110	(MAPbI <sub>3</sub> ) <sub>24</sub>	0.12	1.09	-1.59

Tables S3 and S4: Stoichiometry and surface energy with and without THTO adsorbed for the cubic (S2) and tetragonal (S3) MAPbI<sub>3</sub> surfaces. Surface energies were calculated at  $\Delta\mu_{\text{Pb}} = -1.5$  and  $\Delta\mu_{\text{I}} = -0.6$

### Different morphology of films from THTO method and interdiffusion method

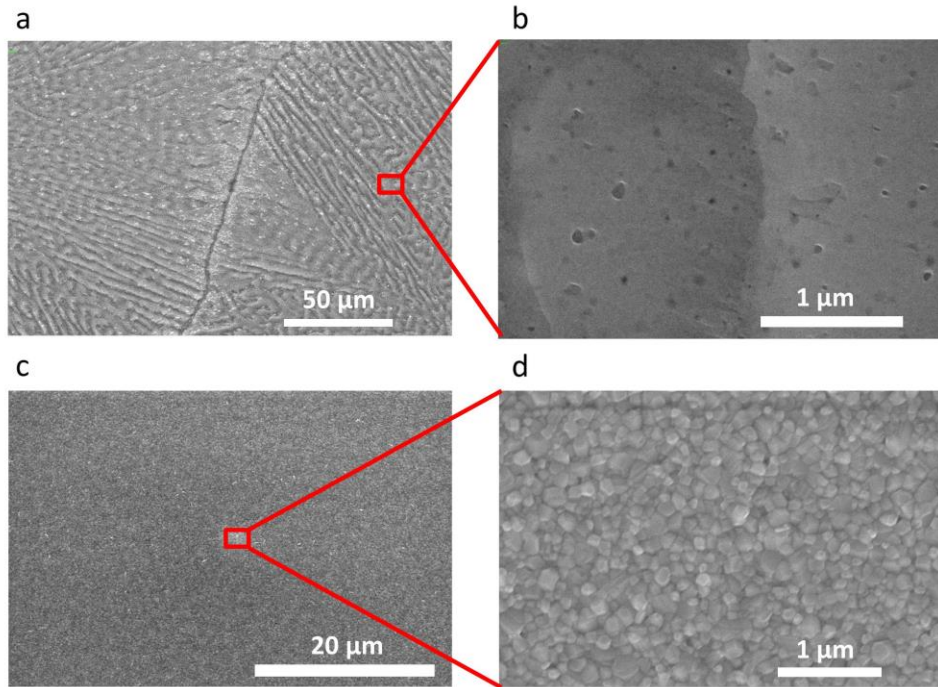


**Figure S.14.** Comparison of SEM pictures of (a), (b) tetragonal (100) MAPbI<sub>3</sub> films from the THTO method and (c), (d) randomly oriented MAPbI<sub>3</sub> films from the interdiffusion method.

### Photoluminescence lifetime comparison of films with tetragonal (100) orientation and random orientation

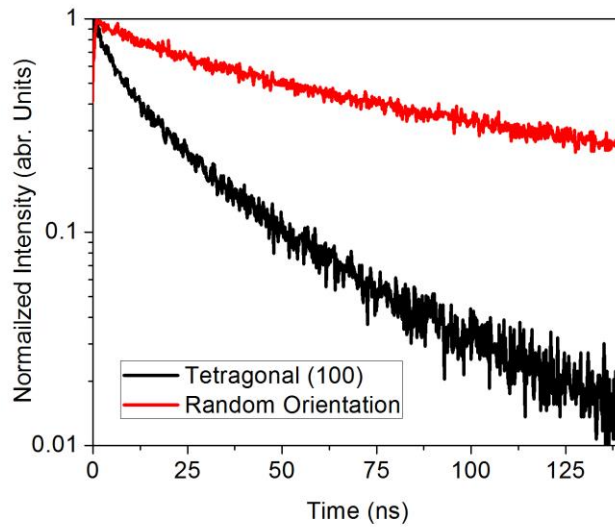


**Figure S.15.** The film with random orientation shows longer photoluminescence lifetime of 260 ns compared to the tetragonal (100) oriented film (10 ns).

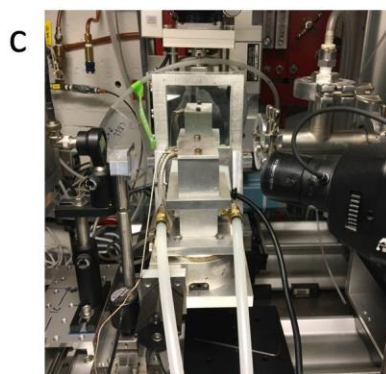
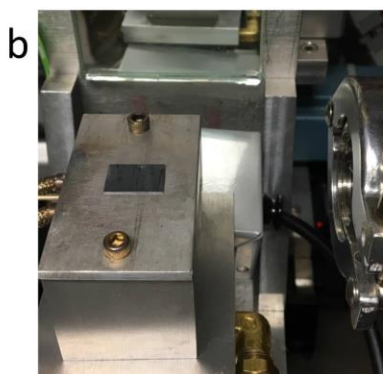
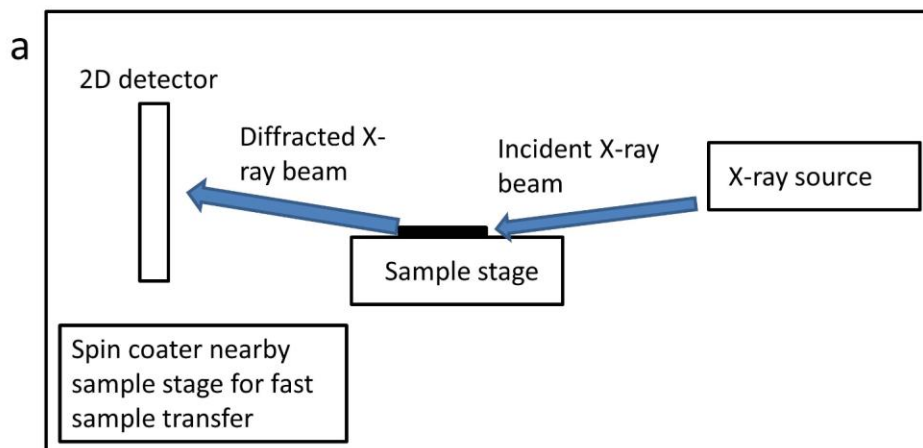


**Figure S.16.** (a) schematic of *in-situ* X-ray diffraction experimental setup (b), (c) pictures of the sample stage.

### References

1. M. Saliba, K. W. Tan, H. Sai, D. T. Moore, T. Scott, W. Zhang, L. A. Estroff, U. Wiesner, H. J. Snaith, *The Journal of Physical Chemistry C* 2014, **118**, 17171.
2. J. Haruyama, K. Sodeyama, L. Han, Y. Tateyama, *J Phys Chem Lett* 2014, **5**, 2903.